

RSC Advances

Accepted Manuscript



This article can be cited before page numbers have been issued, to do this please use: K. Chen, Y. Hao, M. Zhang, D. Zhou, Y. Cao, Y. Wang and L. Feng, *RSC Adv.*, 2016, DOI: 10.1039/C6RA21540H.



This is an Accepted Manuscript, which has been through the Royal Society of Chemistry peer review process and has been accepted for publication.

Accepted Manuscripts are published online shortly after acceptance, before technical editing, formatting and proof reading. Using this free service, authors can make their results available to the community, in citable form, before we publish the edited article. We will replace this Accepted Manuscript with the edited and formatted Advance Article as soon as it is available.

You can find more information about Accepted Manuscripts in the [author guidelines](#).

Please note that technical editing may introduce minor changes to the text and/or graphics, which may alter content. The journal's standard [Terms & Conditions](#) and the ethical guidelines, outlined in our [author and reviewer resource centre](#), still apply. In no event shall the Royal Society of Chemistry be held responsible for any errors or omissions in this Accepted Manuscript or any consequences arising from the use of any information it contains.

catalyst with mesoporous structure shows an excellent ORR performance very comparable to that of commercial Pt/C in alkaline media, probably due to the synergistic effect of the proper heteroatom-doping and its structural advantages.

2. Experimental

2.1. Material Preparation

Crosslinking poly(cyclotriphosphazene-co-4,4'-sulfonyldiphenol) nanospheres (PZS) were prepared according to the method as described in the literatures.^{37,38} Briefly, 1.6 g of phosphonitrilic chloride trimer and 3.455 g of 4,4'-sulfonyldiphenol were dissolved in a acetonitrile solution (160 mL) with ultrasonication. Then, 8 mL triethylamine was added slowly and the reaction mixture was maintained for 10 min with ultrasonication, yielding a solution with white suspensions. Then, the reaction mixture was centrifuged to wipe off the solvent and washed by using ethanol and distilled water. The product of PZS microspheres was freeze-dried in vacuum overnight.

The N, S, P co-doped porous carbon denoted as NSP-PC-1 was obtained through directly pyrolyzing PZS nanospheres at 900 °C for 60 min with a heating rate of 10 °C min⁻¹ and then cooling down to room temperature under N₂ flow. Another co-doped porous carbon of NSP-PC-2 were prepared by heating the mixture of melamine and PZS nanospheres (with a mass ratio of 10:1) in a semiclosed system under N₂ atmosphere for minimizing the elution of decomposed melamine at high temperature. In a typical run, 0.5 g PZS microspheres and 5 g melamine were dispersed in a hot water solution (80 °C) and stirred for more than 2 h. The resulting mixture was freeze-dried in vacuum overnight and pyrolyzed at 900 °C for 60 min under N₂ atmosphere. The final products were washed by ethanol and dried for use.

2.2. Structural Characterizations

The as-prepared carbon catalysts were characterized by the field emission scanning electron microscope (FESEM, Hitachi S-4800) and transmission electron microscope (TEM, FEI Tecnai F20) for the morphology and microstructure identifications. Raman spectra were recorded on a Micro-Raman spectroscopy system (Renishaw inVia-reflex, 532 nm excitation laser). X-ray photoelectron spectroscopy (XPS) studies were carried out with an ESCALAB 250 spectrometer using a monochromated Al K α excitation source. Nitrogen adsorption-desorption isotherms at -196 °C were measured on an adsorption volumetric analyzer ASAP 2020 manufactured by Micromeritics, Inc. (Norcross, Georgia, USA). All samples were degassed at 200 °C overnight prior to adsorption measurements. A part of the N₂ sorption isotherm in the *P/P*₀ range of 0.005–0.05 was fitted to the BET equation to estimate the BET surface area.³⁹ Total pore volume (*V*_{total}) was obtained at a relative pressure of 0.985. The pore size distribution was obtained using the NLDFT model in the Micromeritics ASAP 2020 software package (assuming slit pore geometry). Micropore area (*S*_{micro}) and volume (*V*_{micro}) were calculated using the t-plot method.

2.3. Electrochemical Tests

All electrochemical measurements were performed at room temperature on a potentiostat (CHI 760E, CH Instrument, Shanghai, China) and a rotating ring disk electrode system (RRDE-3A, ALS Co., Ltd, Japan) with a standard three electrode cell. A Pt wire and an Hg/HgO/0.1 M OH⁻ electrode (0.164 V vs NHE) were used as the counter and reference electrode, respectively. A RDE with glassy carbon (GC) disk electrode (4 mm in diameter) and a rotating ring-disk electrode (RRDE, ALS Co., Ltd, Japan) with a Pt ring (5 mm inner diameter and 7 mm outer diameter) and a GC disk (4 mm diameter) are used as the substrate for the working electrodes. Before use, the GC electrodes in RDE/RRDE are polished using aqueous alumina suspension on polishing pad. All electrode potentials were reported relative to the reversible hydrogen electrode (RHE), which were converted from the Hg/HgO/0.1 M OH⁻ electrode according to the formula: $E_{\text{RHE}} = E_{\text{(Hg/HgO)}} + \phi(\text{Hg/HgO}/0.1 \text{ M OH}^-) + 0.0591 \cdot \text{pH}$.⁴⁰

To fabricate the catalyst-modified working electrode, the catalyst ink was prepared by ultrasonically dispersing the as-prepared carbon catalyst (5 mg) in a solution containing 100 μL Nafion (5 wt%) solution and 900 μL deionized water. The Pt/C catalyst (10 wt% Pt on graphitized carbon, Sigma-Aldrich) ink was prepared in the same way. The above prepared catalyst ink was casted onto the fresh surface of the GCE (a diameter of 4 mm). The catalyst loadings on RDE and RRDE were 400 $\mu\text{g cm}^{-2}$ (40 $\mu\text{g}_{\text{Pt}} \text{ cm}^{-2}$ for the Pt/C catalyst).

ORR performance of the catalysts was investigated via cyclic voltammogram (CV) and linear sweep voltammogram (LSV) in either N₂ or O₂ saturated 0.1 M KOH solution. The scan rate was 50 mV s⁻¹ for CV and 10 mV s⁻¹ for LSV tests. Oxygen reduction current was evaluated by subtracting the background capacitive current, which was measured by scanning the electrode in a N₂-saturated 0.1 M KOH solution under the same conditions. The electron transfer number (*n*) was calculated using Koutecky–Levich (K-L) equations:

$$(1) \frac{1}{J} = \frac{1}{J_k} + \frac{1}{J_L} = \frac{1}{J_k} + \frac{1}{B\omega^{1/2}}$$

$$(2) B = 0.20nFC_0D_0^{2/3}\nu^{-1/6}$$

where *J* is the measured current density, *J_k* is the kinetic current density, *B* is the Levich constant, ω is the angular velocity of the rotating electrode, *n* is the overall number of electrons transferred in the ORR process, *F* is the Faraday constant (96485 C mol⁻¹), *C₀* is the bulk concentration (1.2×10^{-3} mol L⁻¹) of O₂, *D₀* is the diffusion coefficient (1.9×10^{-5} cm² s⁻¹) of O₂ in the KOH solution, and ν is the kinetic viscosity (0.01 cm² s⁻¹) of the electrolyte.⁴¹

Rotating ring-disk electrode (RRDE) tests for ORR were measured in the O₂ saturated 0.1 M KOH solution with a scan rate of 10 mV s⁻¹, and the ring potential was set at 0.7 V for H₂O₂ production.⁴⁰ The electron transfer number *n* and the production yield of HO₂⁻ (HO₂⁻ %) were determined by the following equations:

$$(3) \text{HO}_2^- \% = 200 \times \frac{I_r / N}{I_d + I_r / N}$$

$$(4) n = 4 \times \frac{I_d}{I_d + I_r / N}$$



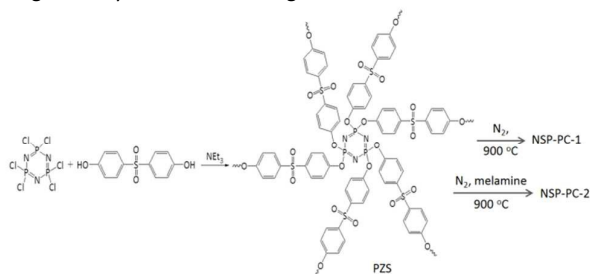
where I_d is the disk current, I_r is the ring current, and N is the current collection efficiency of the Pt ring, which was 0.424 provided by the manufacturer.

Durability of catalysts was evaluated from the i-t chronoamperometric responses of as-prepared carbon catalyst and Pt/C catalyst in O₂-saturated 0.1 M KOH at 0.6 V (vs RHE) for 5.5 h with a rotation rate of 400 rpm. For fuel crossover effect tests, the chronoamperometric response at 0.6 V (vs RHE) was recorded by RDE tests with a rotation rate of 1600 rpm, and followed by the introduction of methanol (3 M) into 0.1 M KOH solution.

3. Results and discussion

The catalysts NSP-PC-1 and NSP-PC-2 were prepared through a two-step method (Scheme 1): (1) Highly cross-linked PZS nanospheres were prepared according to the literature-reported method;^{37,38} (2) The as-prepared PZS nanospheres were carbonized at 900 °C with or without the presence of melamine under N₂ atmosphere to form N, S, P co-doped carbon catalysts. Particularly, PZS nanospheres act as carbon source and N, S, P-doping sources, which might result in a uniform distribution of N, S, P heteroatoms in the carbon catalyst and simplify the preparation. In the case of NSP-PC-2, melamine was added during pyrolysis for additional N-doping and porosity adjustment. The following mechanism has been proposed: in the temperature range of 300–600 °C, melamine is decomposed into carbon nitrides,⁴² which diffuses into the matrix of semi-carbonized PZS. At a higher temperature (i.e., >750 °C), carbon nitrides are further decomposed into N₂, NH₃ and some reactive species (i.e., C₂N₂⁺, C₃N₂⁺, C₃N₃⁺),⁴³⁻⁴⁶ which are released from or react with the carbon matrix to contribute to the porosity adjustment or to introduce the N-containing functionalities in the carbon product.⁴⁷

The structures and morphologies of the as-prepared catalysts were investigated by scanning electron microscopy (SEM) and transmission electron microscopy (TEM). As shown in SEM images (Fig. 1), NSP-PC-2 has a sheet-like morphology, unlike the nanospherical morphology of NSP-PC-1 or PZS (see Fig. S1a). Thus, the formation of the sheet-like structures of NSP-PC-2 might be attributed to the presence of melamine during pyrolysis, though the mechanism is still unknown. The TEM image in Fig. 2a also reveals the sheet-like feature of NSP-PC-2. Furthermore, a high-resolution (HR)TEM image (Fig. 2b) suggests that NSP-PC-2 is amorphous in nature. Fig. 2c shows a typical scanning transmission electron microscopy (STEM) annular dark field (ADF) image and elemental mapping of NSP-PC-2, where all the elements (C, O, N, P and S) are homogeneously distributed throughout the carbon nanosheet.



Scheme 1. Preparations of NSP-PC-1 and NSP-PC-2.

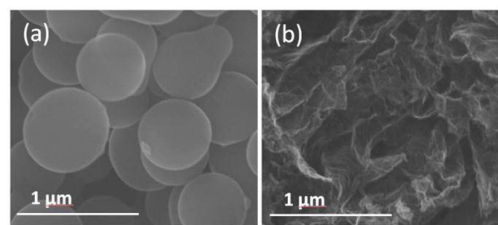


Fig. 1. SEM images of (a) NSP-PC-1, (b) NSP-PC-2.

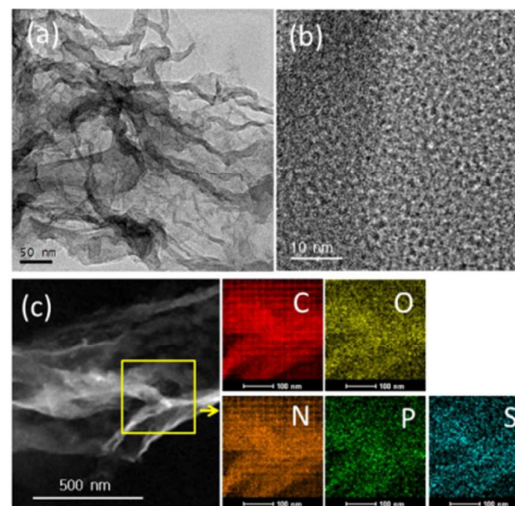


Fig. 2. (a,b) TEM and HRTEM images of NSP-PC-2. (c) HADDF image and compositional EDS mapping of NSP-PC-2 using scanning transmission electron microscopy.

The X-ray photoelectron spectroscopy (XPS) analysis (Fig. 3 and Fig. S2) further reveals the N, S, P-codoping in the catalyst NSP-PC-2 as well as NSP-PC-1. Particularly, the N 1s spectrum demonstrates three types of N species in NSP-PC-2, corresponding to graphitic-N (401.0 eV),⁴⁸ pyrrolic-N (399.8 eV),⁴⁹ and pyridinic-N or P=N/P-N (398.2 eV). Among them, graphitic-N, pyrrolic-N and pyridinic-N or P=N/P-N are all considered to be favorable for ORR.⁵⁰⁻⁵³ The S 2p spectrum reveals only thiophene-S in NSP-PC-2, which is also believed to play an important role in enhancing catalytic activity. The two peaks positioned at 165.1 and 163.9 eV are consistent with the S 2p_{1/2} and S 2p_{3/2} of thiophene-S, owing to their spin-orbit coupling.^{54,55} The P 2p spectrum can be fitted with two peaks at 132.6 and 133.6 eV, corresponding to P-C and P=N/P-N bonding, respectively,^{51,56} indicating that P atoms were incorporated into the N-doped carbon framework. Such a doping way was found to create more active sites and trigger synergistic effects for ORR electrocatalysis.¹⁶ NSP-PC-1 also exhibits similar XPS spectra (Fig. S2). However, the N, S, P contents of the carbon catalysts are very different (see Table S1 in ESI). Particularly, NSP-PC-2 has 9.05 at.% N, 0.6 at.% S and 1 at.% P, while NSP-PC-1 has 3.75 at.% N, 4 at.% S and 0.1 at.% P. The higher N-content and lower S-content in NSP-PC-2 may be attributed to the additional precursor of melamine, which not only provides additional N source but also results in desulfurization to some extent.⁵⁷ On the other hand, the higher P content in NSP-PC-2 might be related to the increase of N-doping.



As suggested in P 2p spectrum (Fig. 3), the higher P-doping in NSP-PC-2 occurs with bonding configuration of C-P=N/C-P-N.

Raman spectroscopy is adopted to further investigate the structural feature of the carbon catalysts. As shown in Fig. S4 (in ESI), the two characteristic peaks at around 1350 and 1580 cm^{-1} are assigned to the D band and G band, respectively, confirming the presence of disordered carbon and graphitic carbon.⁵⁸ Particularly, NSP-PC-1 and NSP-PC-2 show similar I_D/I_G band intensity ratio (i.e., 0.925 and 0.923), indicating their similar disorder degree in spite of their different pyrolysis conditions (i.e., with or without melamine).

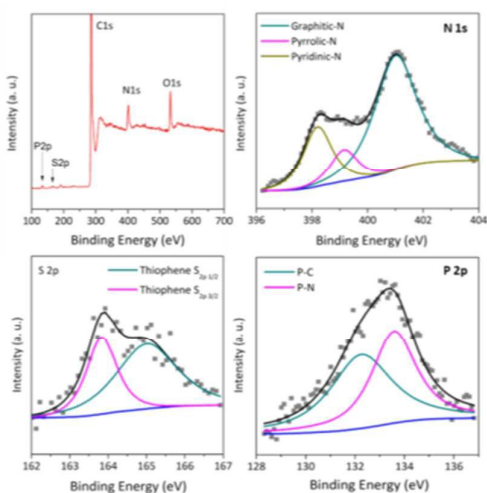


Fig. 3. XPS spectra of NSP-PC-2.

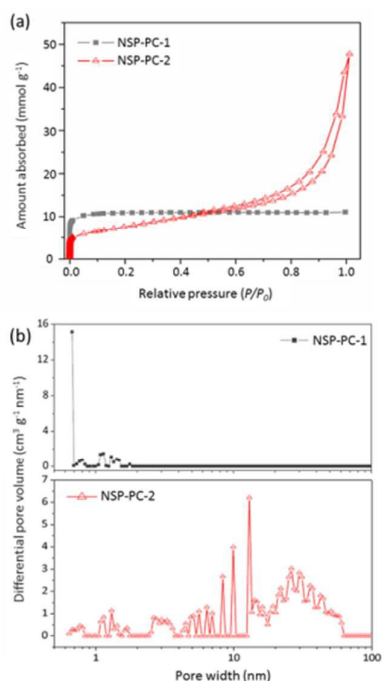


Fig. 4. (a) N_2 adsorption-desorption isotherms and (b) pore size distributions of NSP-PC-1 and NSP-PC-2 calculated using NLDFT.

Table 1. Textural properties of NSP-PC-1 and NSP-PC-2, compared with those of control catalysts N-PC-1 and NSP-PC-3.

Catalysts	S_{BET} (m^2g^{-1}) ^a	V_{total} (cm^3g^{-1})	S_{micro} (m^2g^{-1})	V_{micro} (cm^3g^{-1})	S_{meso} (m^2g^{-1})	V_{meso} (cm^3g^{-1})
NSP-PC-1	967	0.38	898	0.346	69	0.036
N-PC-1	845	0.33	807	0.307	38	0.023
NSP-PC-2	613	1.42	49	0.019	564	1.40
NSP-PC-3	648	1.56	27	0.009	621	1.55

^a Surface areas (S_{BET}) were calculated by the BET method.

^b The total pore volumes (V_{total}) were estimated from the adsorbed amount at a relative pressure $P/P_0 = 0.985$.

^c Micropore area (S_{micro}) and volume (V_{micro}) were calculated using the t-plot method.

^d Mesopore areas (S_{meso}) and volume (V_{meso}) were calculated from the difference of the BET surface area and micropore area ($S_{\text{meso}} = S_{\text{BET}} - S_{\text{micro}}$), and the total pore volume and micropore volume ($V_{\text{meso}} = V_{\text{total}} - V_{\text{micro}}$), respectively.

The porous characteristics of the catalysts NSP-PC-2 and NSP-PC-1 were investigated by N_2 adsorption-desorption measurements. The textural properties were summarized in Table 1. As presented in Fig. 4a, NSP-PC-2 presents a typical type-IV isotherm according to the IUPAC classification, which shows a small N_2 uptake at low relative pressure ($P/P_0 < 0.001$), a clear hysteresis loop and an evident rise in the medium and high pressure regions ($P/P_0 = 0.8-1.0$), indicative of mainly mesoporous structures with a moderately high BET surface area of $613 \text{ m}^2 \text{ g}^{-1}$ and a large pore volume of $1.42 \text{ cm}^3 \text{ g}^{-1}$. In contrast, the isotherm for NSP-PC-1 is assigned to type-I, suggesting sheer microporous structures (up to 93% microporosity) with a high BET surface area of $967 \text{ m}^2 \text{ g}^{-1}$ and a pore volume of $0.38 \text{ cm}^3 \text{ g}^{-1}$. The different porosities of these carbon catalysts were also demonstrated by pore size distribution (PSD) results calculated using NLDFT method. As shown in Fig. 4b, the pore volume of NSP-PC-1 is mainly contributed by the micropores (with sizes smaller than 2 nm), while the porosity of NSP-PC-2 is mainly distributed into a mesopore system with sizes ranging from 2.5 nm to 50 nm ($\sim 90\%$ mesoporosity). Thus, it appears that the melamine plays a significant role in achieving the mesoporosity of NSP-PC-2. This may be attributed to the generation of gaseous agents (i.e., N_2 and NH_3) due to the decomposition of melamine or its derivative (i.e., carbon nitride) at high temperature (i.e., 900 $^\circ\text{C}$),^{44,45} which might swell the carbon matrix and induces the formation of mesopores.

The ORR catalytic activity of the catalysts NSP-PC-1 and NSP-PC-2 was first assessed by means of cyclic voltammetry (CV) and linear sweep voltammetry (LSV) in 0.1 M KOH solution saturated with O_2 . In order to better understand the catalytic performances and reveal the role of heteroatom-doping, a control catalyst was prepared by pyrolyzing melamine-doped polymeric nanospheres,^{59,60} noted as N-PC-1 (see ESI for preparation details). Though N-PC-1 was derived from the precursor different from that of NSP-PC-1, its structural features including the nanospherical morphology, microporous characteristics and BET area are very similar to those of NSP-PC-1 (see Fig. S1a, S5 in ESI and Table 1). Moreover, as suggested by XPS analysis, N-PC-1 contains no S, P but only N species. The identified N-compositions and content in N-PC-1 are similar to those found in NSP-PC-1. (Fig. S3 and Table S1 in ESI).

As shown in Fig. 5a, the CV results indicate that the control catalyst N-PC-1 shows a poorer ORR catalytic activity in terms of the



more negative oxygen reduction peak potential as compared to that of NSP-PC-1 or NSP-PC-2. This trend is again demonstrated by the LSV results (Fig. 5b). The control catalyst N-PC-1 exhibits an apparently less enhanced catalytic activity for ORR in view of an $E_{1/2}$ of 0.71 V, which is 70 and 140 mV lower than those of N, S, P co-doped catalysts NSP-PC-1 and NSP-PC-2, respectively. Considering the similar structural features of N-PC-1 and NSP-PC-1, the better catalytic activity of the latter can be safely attributed to the contribution of additional S, P-doping. It is also clear seen that the catalyst NSP-PC-2 shows the best catalytic activity among three as-prepared carbon catalysts in terms of the most positive $E_{1/2}$ of 0.85 V. The improved catalytic activity of NSP-PC-2 relative to that of NSP-PC-1 might be due to its slightly higher overall NSP content and more importantly, the distinct structural feature (such as the mesoporosity), which makes the active sites very accessible for the reactants and facilitates the mass-transfer despite of the lower surface area of NSP-PC-2 relative to that of microporous NSP-PC-1.

To further explore the effect of the dosage of introduced heteroatoms on the electrocatalytic activity of the as-prepared carbon catalyst, another control catalyst NSP-PC-3 was prepared by the same synthetic route as NSP-PC-2 except for lower pyrolysis temperature (i.e., 800 °C). As suggested by N_2 adsorption-desorption measurement, Raman and XPS analysis (see Fig. S1b, S4, S6, S7 and Table S1 in ESI), NSP-PC-3 exhibits similar structural feature as that of NSP-PC-2 but much higher overall NSP content. However, NSP-PC-3 shows a poorer catalytic activity in terms of smaller diffusion limiting current density and an $E_{1/2}$ at 0.83 V, which is 20 mV lower than that of NSP-PC-2 (see Fig. 5d). Such a

degraded catalytic performance might be attributed to the reduction of electrical conductivity with higher NPS content, which obstructs the ORR process in NSP-PC-3.

It is noteworthy that the $E_{1/2}$ of NSP-PC-2 is even 10 mV higher than that of the commercial Pt/C catalyst (i.e., a value of 0.84 V comparable to the reference data with similar Pt loading),⁶¹⁻⁶³ suggesting an excellent ORR activity for NSP-PC-2. This $E_{1/2}$ value is also more positive than those of recently reported NSP-codoped porous carbons, which are remarkably lower than that of commercial Pt/C catalyst.^{27,28} The K-L plots (J^{-1} vs. $\omega^{-1/2}$ in Fig. 5e and S11) derived from the LSVs of NSP-PC-2 show an excellent linearity, implying a first-order reaction in this potential range. The calculated average electron-transfer number (n) is 3.84. This value is close to that obtained from the rotating ring-disk electrode (RRDE) measurements ($n=4.02\sim 3.99$, see Fig. 5f), suggesting a one-step, four-electron oxygen reduction process for this carbon catalyst. The RRDE measurements also reveal that the production of HO_2^- was suppressed on the catalyst NSP-PC-2 with a yield below $\sim 7.3\%$ over the potential range of 0.4~0.9 V (see Fig. S12 in ESI), which is closely comparable to that reported for Pt/C catalyst (4-5%).³⁰ Moreover, the Tafel slope of NSP-PC-2 was calculated to be 84.1 mV dec^{-1} (see Fig. S13 in ESI), very close to that of Pt/C (83.8 mV dec^{-1}) measured under the same condition, indicating the transfer of the first electron is probably the rate-determining step in ORR catalyzed by NSP-PC-2, similar to platinum.⁶⁴ Thus, all these results suggest an excellent ORR activity for the catalyst NSP-PC-2, which is very comparable to that of commercial Pt/C catalyst.

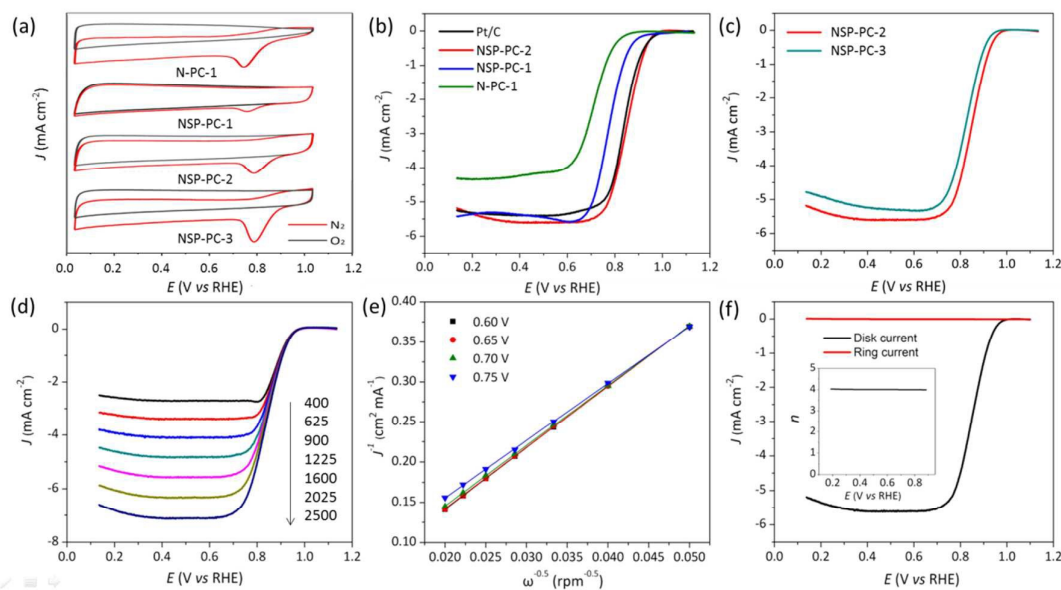


Fig. 5. (a) CV curves of different carbon catalysts recorded in O_2 -saturated (red line) or N_2 -saturated (black line) in 0.1 M KOH. (b, c) LSV curves of NSP-PC-1 and NSP-PC-2 compared to Pt/C and control catalysts in O_2 -saturated 0.1 M KOH at 1600 rpm. (d) LSV curves of NSP-PC-2 at different rotation speeds (rpm) in 0.1 M KOH. (e) The Koutecky-Levich (K-L) plots for NSP-PC-2 at different potentials (see Fig. S11 for theoretical K-L plots for 2 and 4 electron-transfer, respectively). (f) RRDE test of the ORR on NSP-PC-2 in O_2 -saturated 0.1 M KOH at 1600 rpm. The inset shows the n value against electrode potential. The loading of all nonprecious catalysts is $400 \mu g_{Pt} cm^{-2}$. The Pt loading is $40 \mu g_{Pt} cm^{-2}$.



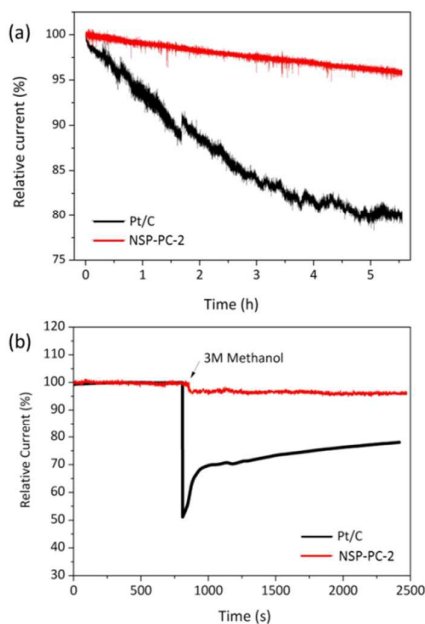


Fig. 6. (a) The durability of the catalyst-modified electrodes for the ORR in oxygen-saturated 0.1 M KOH. (b) *i-t* chronoamperometric responses of the catalyst-modified electrodes at 0.6 V (vs RHE) with a rotating speed of 1600 rpm in oxygen-saturated 0.1 M KOH. The arrow indicates the addition of methanol into the electrolytic cell.

The durability and possible fuel crossover effect are also important for cathodic catalysts in fuel cells. The durability of the NSP-PC-2 was examined via a continuous chronoamperometric measurement and compared to that of Pt/C catalyst. As shown in Fig. 6a, the Pt/C modified electrode suffers a 20% current decay after 5.5 h, while only a small current decay of 5% is observed for NSP-PC-2-modified electrode, indicating much better stability of this carbon catalyst in an alkaline environment. This result was confirmed by a repeated potentiodynamic cycling durability test. As shown in Figure S14, a slightly shifted LSV curve ($\Delta E_{1/2}=10$ mV) was observed for NPS-PC-2 after 5000 CV cycles between 0.6 to 1.0 V, while there was a 40 mV loss of half-wave potential for the Pt/C catalyst under the same conditions. Moreover, the current density of NPS-PC-2 is almost unchanged upon CV cycling, indicating that surface properties were maintained during potential cycling tests.⁶⁵⁻⁶⁷ In addition, the methanol crossover effect on NSP-PC-2 was evaluated using chronoamperometric measurements. As shown in Fig. 6b, upon the addition of 3 M methanol, Pt/C electrode presents a significant drop of ca. 50% in the ORR current, whereas no noticeable change is observed for the NSP-PC-2-modified electrode. This result suggests that the catalyst NSP-PC-2 has a greater tolerance to methanol crossover than the commercial Pt/C catalyst.

4. Conclusions

In summary, starting with PZS nanospheres as the single precursors, we have developed N, S, P-codoped carbons (i.e., NSP-PC-1 and NSP-PC-2) with either micro- or mesoporosity as efficient and stable ORR electrocatalysts. As the microporous catalyst NSP-

PC-1 exhibits a significantly enhanced ORR catalytic activity compared to solely N-doped counterpart, it unambiguously suggests that additional S, P-doping can dramatically promote the ORR activity of carbon catalyst. Moreover, the mesoporous catalyst NSP-PC-2 shows an optimal catalytic activity in terms of an $E_{1/2}$ at 0.85 V (vs RHE) in alkaline media, which is closely comparable to that of Pt/C and 70 mV higher than that of microporous NSP-PC-1. The superior catalytic activity of NSP-PC-2 is mainly attributed to its proper N, S, P-codoping (~11at.%) as well as its structural advantages such as the high mesoporosity and moderately high surface area ($613\text{ m}^2\text{g}^{-1}$), which might make the active sites very accessible and facilitates the O_2 mass transfer.

Acknowledgements

This work is supported in part by the Natural Science Foundation of China (51372158), Jiangsu Specially Appointed Professor Program (SR10800113), and the Project for Jiangsu Scientific and Technological Innovation Team (2013).

Notes and references

- B.C. Steele and H.A. Heinzel, *Nature*, 2001, **414**, 345–352.
- M. Nesselberger, M. Roefzaad, R.F. Hamou, P.U. Biedermann, F.F. Schweinberger, S. Kunz, K. Schloegl, G.K.H. Wiberg, S. Ashton, U. Heiz, K.J.J. Mayrhofer and M. Arenz, *Nat. Mater.*, 2013, **12**, 919–924.
- A. Anastasopoulos, J.C. Davies, L. Hannah, B.E. Hayden, C.E. Lee, C. Milhano, C. Mormiche and L. Offin, *ChemSusChem*, 2013, **6**, 1973–1982.
- J. Wu, M. Shi, X. Yin and H. Yang, *ChemSusChem*, 2013, **6**, 1888–1892.
- D. Wang, H.L. Xin, R. Hovden, H. Wang, Y. Yu, D.A. Muller, F.J. DiSalvo and H.D. Abruña, *Nat. Mater.*, 2013, **12**, 81–87.
- M. Shao, Q. Chang, J.-P. Dodelet and R. Chenitz, *Chem. Rev.*, 2016, **116**, 3594–3657.
- D. Yu, E. Nagelli, F. Du and L. Dai, *J. Phys. Chem. Lett.*, 2010, **1**, 2165–2173.
- N. Alonso-Vante, *ChemPhysChem*, 2010, **11**, 2732–2744.
- X. Yu and S. Ye, *J. Power Sources.*, 2007, **172**, 145–154.
- X. Tong, S. Chen, C. Guo, X. Xia and X.-Y. Guo, *ACS Appl. Mater. Interfaces.*, 2016, DOI: 10.1021/acsami.5b10044.
- J. Wu, R. Mi, S. Li, P. Guo, J. Mei, H. Liu, W. Lau and L. Liu, *RSC Adv*, 2015, **5**, 25304–25311.
- G. Tao, L. Zhang, L. Chen, X. Cui, Z. Hua, M. Wang, J. Wang, Y. Chen and J. Shi, *Carbon*, 2015, **86**, 108–117.
- K.-H. Wu, D.-W. Wang, D.-S. Su and I.R. Gentle, *ChemSusChem*, 2015, **8**, 2772–2788.
- P. Trogadas, T.F. Fuller and P. Strasser, *Carbon*, 2014, **75**, 5–42.
- Y. Ito, H.-J. Qiu, T. Fujita, Y. Tanabe, K. Tanigaki and M. Chen, *Adv. Mater.*, 2014, **26**, 4145–4150.
- R. Li, Z. Wei and X. Gou, *ACS Catal*, 2015, **5**, 4133–4142.
- Y. Liang, Y. Li, H. Wang, J. Zhou, J. Wang, T. Regier and H. Dai, *Nat. Mater.*, 2011, **10**, 780–786.
- G. Zhang, B.Y. Xia, X. Wang and X.W. Lou, *Adv. Mater.*, 2014, **26**, 2408–2412.



19. Y. Gao, H. Zhao, D. Chen, C. Chen and F. Ciucci, *Carbon*, 2015, **94**, 1028–1036.
20. D.-W. Wang and D. Su, *Energy Environ. Sci.*, 2014, **7**, 576–591.
21. J.P. Paraknowitsch and A. Thomas, *Energy Environ. Sci.*, 2013, **6**, 2839–2855.
22. W. Xiong, F. Du, Y. Liu, A. Perez Jr, M. Supp, T.S. Ramakrishnan, L.M. Dai and L. Jiang, *J. Am. Chem. Soc.*, 2010, **132**, 15839–15841.
23. Y. L. Zhu, C. Su, X.M. Xu, W. Zhou, R. Ran and Z.P.A. Shao, *Chem.–Eur. J.*, 2014, **20**, 15533–15542.
24. Y. Zheng, Y. Jiao, M. Jaroniec, Y. Jin and S.Z. Qiao, *Small*, 2012, **8**, 3550–3566.
25. W. Ai, Z.M. Luo, J. Jiang, J.H. Zhu, Z.Z. Du, Z.X. Fan, L.H. Xie, H. Zhang, W. Huang and T. Yu, *Adv. Mater.*, 2014, **26**, 6186–6192.
26. J. Liang, Y. Jiao, M. Jaroniec and S.Z. Qiao, *Angew. Chem. Int. Ed.*, 2012, **51**, 11496–11500.
27. S. Gao, X. Wei, H. Liu, K. Geng, H. Wang, H. Moehwald and D. Shchukin, *J. Mater. Chem. A*, 2015, **3**, 23376–23384.
28. J. Wu, X. Zheng, C. Jin, J. Tian and R. Yang, *Carbon*, 2015, **92**, 327–338.
29. C.H. Choi, S.H. Park and S.I. Woo, *ACS Nano*, 2012, **6**, 7084–7091.
30. Y. Gong, H. Fei, X. Zou, W. Zhou, S. Yang, G. Ye, Z. Liu, Z. Peng, J. Lou, R. Vajtai, B.I. Yakobson, J.M. Tour and P.M. Ajayan, *Chem. Mater.*, 2015, **27**, 1181–1186.
31. D. Eisenberg, W. Stroek, N.J. Geels, C.S. Sandu, A. Heller, N. Yan and G.A. Rothenberg, *Chem. Eur. J.*, 2016, **22**, 501–505.
32. G.A. Ferrero, K. Preuss, A.B. Fuertes, M. Sevilla and M.-M. Titirici, *J. Mater. Chem. A*, 2016, **4**, 2581–2589.
33. N. Daems, X. Sheng, I.F.J. Vankelecom and P.P. Pescarmona, *J. Mater. Chem. A*, 2014, **2**, 4085–4110.
34. X. Zhao, H. Zhao, T. Zhang, X. Yan, Y. Yuan, H. Zhang, H. Zhao, D. Zhang, G. Zhu and X. Yao, *J. Mater. Chem. A*, 2014, **2**, 11666–11671.
35. J.-Y. Choi, R.S. Hsu and Z. Chen, *J. Phys. Chem. C*, 2010, **114**, 8048–8053.
36. Y. He, X. Han, Y. Du, B. Song, P. Xu and B. Zhang, *ACS Appl. Mater. Interfaces*, 2016, **8**, 3601–3608.
37. J. Zhou, L. Meng, X. Feng, X. Zhang and Q. Lu, *Angew. Chem. Int. Ed.*, 2010, **49**, 8476–8479.
38. S. Yang, L. Peng, P. Huang, X. Wang, Y. Sun, C. Cao and W. Song, *Angew. Chem. Int. Ed.*, 2016, **55**, 647–648.
39. K.S. Walton and R.Q. Snurr, *J. Am. Chem. Soc.*, 2007, **129**, 8552–8556.
40. J. Guo, A. Hsu, D. Chu and R. Chen, *J. Phys. Chem. C*, 2010, **114**, 4324–4330.
41. S. Yang, X. Feng, X. Wang and K. Müllen, *Angew. Chem. Int. Ed.*, 2011, **50**, 5339–5343.
42. M. Groenewolt, M. Antonietti, *Adv. Mater.*, 2005, **17**, 1789–1792.
43. Z.-H. Sheng, L. Shao, J.-J. Chen, W.-J. Bao, F.-B. Wang and X.-H. Xia, *ACS Nano*, 2011, **5**, 4350–4358.
44. S. Trasobares, C. Kolczewski, R.R. 1ty, N. Borglund, A. Bassan, G. Hug, C. Colliex, S. Csillag, L. G.M. Pettersson, *J. Phys. Chem. A*, 2003, **107**, 228–235.
45. S. Ju, C. Han, C. Wu, M. Mebel, Y. Chen, *J. Phys. Chem. B*, 1999, **103**, 582–596.
46. A.B. Fuertes, G.A. Ferrero and M. Sevilla, *J. Mater. Chem. A*, 2014, **2**, 14439–14448.
47. W.-H. Lee and J.H. Moon, *ACS Appl. Mater. Interfaces*, 2014, **6**, 13968–13976.
48. H.L. Peng, Z.Y. Mo, S.J. Liao, H.G. Liang, L.J. Yang and F. Luo, *Sci. Rep.*, 2013, **3**, 1765.
49. R.L. Liu, D.Q. Wu, X.L. Feng and K. Mullen, *Angew. Chem. Int. Ed.*, 2010, **49**, 2565–2569.
50. C. Wang, L. Sun, Y. Zhou, P. Wan, X. Zhang and J. Qiu, *Carbon*, 2013, **59**, 537–546.
51. F. Razmjooei, K.P. Singh, M.Y. Song and J.-S. Yu, *Carbon*, 2014, **78**, 257–267.
52. D.S. Yang, D. Bhattacharjya, S. Inamdar, J. Park and J.S. Yu, *J. Am. Chem. Soc.*, 2012, **134**, 16127–16130.
53. T.Y. Ma, J. Ran, S. Dai, M. Jaroniec and S.Z. Qiao, *Angew. Chem. Int. Ed.*, 2015, **54**, 4646–4650.
54. Y.H. Bing, H.S. Liu, L. Zhang, D. Ghosh and J.J. Zhang, *Chem. Soc. Rev.*, 2010, **39**, 2184–2202.
55. J. Xu, G. Dong, C. Jin, M. Huang and L. Guan, *ChemSusChem*, 2013, **6**, 493–499.
56. H. Jiang, Y. Zhu, Q. Feng, Y. Su, X. Yang and C. Li, *Chem. Eur. J.*, 2014, **20**, 3106–3112.
57. J. Xiao, Y. Zhang, Q. Zhong, F. Li, J. Huang and B. Wang, *Energy Fuels*, 2016, **30**, 3385–3391.
58. B. You, N. Jiang, M. Sheng, W.S. Drisdell, J. Yano and Y. Sun, *ACS Catal.*, 2015, **5**, 7068–7076.
59. H. Cong, M. Zhang, Y. Chen, K. Chen, Y. Hao, Y. Zhao and L. Feng, *Carbon*, 2015, **92**, 297–304.
60. H. Zhou, S. Xu, H. Su, M. Wang, W. Qiao and L. Ling, *Chem. Commun.*, 2013, **49**, 3763–3765.
61. H. Ba, Y. Liu, L. Truong-Phuoc, C. Duong-Viet, J.-M. Nhut, D.L. Nguyen, O. Ersen, G. Tuci, G. Giambastiani and C. Pham-Huu, *ACS Catal.*, 2016, **6**, 1408–1419.
62. C. Guo, W. Liao, Z. Li, L. Sun and C. Chen, *Nanoscale*, 2015, **7**, 15990–15998.
63. B.Y. Xia, Y. Yan, N. Li, H.B. Wu, X.W. Lou and X. Wang, *Nat. Energy.*, 2016, DOI: 10.1038/NENERGY.2015.6.
64. Y. Li, W. Zhou, H. Wang, L. Xie, Y. Liang, F. Wei, J.-C. Idrobo, S.J. Pennycook and H. Dai, *Nat. Nanotechnol.*, 2012, **7**, 394–400.
65. J. Sanetuntikul, T. Hang and S. Shanmugam, *Chem. Commun.*, 2014, **50**, 9473–9476.
66. J. Sanetuntikul, K. Ketpang, and S. Shanmugam, *ACS Catal.*, 2015, **5**, 7321–7327.
67. J. Sanetuntikul, C. Chuaicham, Y.-W. Choi and S. Shanmugam, *J. Mater. Chem. A*, 2015, **3**, 15473–15481.



TOC

View Article Online
DOI: 10.1039/C6RA21540H

The N/S/P-codoped carbon catalysts with varied nanostructures were facilely prepared. The mesoporous carbon nanosheets exhibit the optimal catalytic activity for ORR.

